Smart Materials and Structures

**PAPER** • **OPEN ACCESS**

# Adaptive piezoelectric metamaterial beam: autonomous attenuation zone adjustment in complex vibration environments

To cite this article: Yupei Jian *et al* 2023 *Smart Mater. Struct.* **32** 105023

View the article online for updates and enhancements.

You may also like

- High-fidelity dynamics of piezoelectric covered metamaterial Timoshenko beams using the spectral element method
  Guobiao Hu, Lihua Tang, Yaowen Yang et al.
- Methods for the Integration of New Architectural Nanostructures with MEMS Systems for Sensors and Harvester Devices
  Mariuca Gartner, Mariana Chelu, Hermine Stroescu et al.
- Modal analysis of finite-size piezoelectric metamaterial plates
  Amirreza Aghakhani, Mehmet Murat Gozum and Ipek Basdogan

PRIME PACIFIC RIM MEETING ON ELECTROCHEMICAL AND SOLID STATE SCIENCE
HONOLULU,HI
October 6-11, 2024
Joint International Meeting of
The Electrochemical Society of Japan (ECSJ)
The Korean Electrochemical Society (KECS)
The Electrochemical Society (ECS)
Early Registration Deadline:
September 3, 2024
MAKE YOUR PLANS NOW!

This content was downloaded from IP address 213.218.254.40 on 01/08/2024 at 14:11

OPEN ACCESS
IOP Publishing
Smart Materials and Structures
Smart Mater. Struct. **32** (2023) 105023 (15pp)
https://doi.org/10.1088/1361-665X/acf62f

# Adaptive piezoelectric metamaterial beam: autonomous attenuation zone adjustment in complex vibration environments

**Yupei Jian[1,2], Guobiao Hu[3], Lihua Tang[2,*], Yincheng Shen[2], Yulin Zhan[4] and Kean Aw[2]**

[1] School of Electrical Engineering, Southwest Jiaotong University, Chengdu, Sichuan 610031, People's Republic of China
[2] Department of Mechanical and Mechatronics Engineering, The University of Auckland, Auckland 1010, New Zealand
[3] Internet of Things Thrust, The Hong Kong University of Science and Technology (Guangzhou), Guangzhou, Guangdong 511400, People's Republic of China
[4] School of Civil Engineering, Southwest Jiaotong University, Chengdu, Sichuan 610031, People's Republic of China

E-mail: l.tang@auckland.ac.nz

Received 15 May 2023, revised 19 August 2023
Accepted for publication 1 September 2023
Published 11 September 2023

## Abstract

Programmable metamaterials for broadband vibration control draw growing interest due to their abilities to tailor dynamic responses. However, the deterministic dynamic behavior of any traditional metamaterial is a challenge to cope with the complex and variable vibration conditions in real environments. This work proposes an adaptive piezoelectric metamaterial beam (piezo-meta-beam) that consists of bimorph piezoelectric arrays. The shunt circuits are designed with self-tuning abilities by integrating microcontroller-driven digital potentiometers into synthetic inductive circuits. Two typical scenarios are considered, i.e., harmonic and white noise excitations with different spectra. Different self-tuning strategies based on bandgap prediction are contrapuntally developed. However, a flaw in the analytical bandgap expression widely appearing in the literature is noted through a verification study. A modified bandgap expression based on the 3D finite element model is proposed for correction. This modified bandgap expression is adopted in formulating the control strategy of the microcontroller. A series of experiments are conducted to investigate the adaptive behavior of the piezo-meta-beam. In the harmonic sweep excitation test, the adaptive piezo-meta-beam shows an ultra-broad attenuation zone (220–720 Hz), while the traditional counterpart only has a bandgap width of less than 20 Hz. In the case of noise excitation, autonomous adjustment of the center frequency and attenuation zone is achieved for noises over different spectra. In general, this work presents a methodology for designing intelligent metamaterials that can adapt to environmental vibrations with vast potential for real applications.

---

[*] Author to whom any correspondence should be addressed.

Original content from this work may be used under the terms of the Creative Commons Attribution 4.0 licence. Any further distribution of this work must maintain attribution to the author(s) and the title of the work, journal citation and DOI.

© 2023 The Author(s). Published by IOP Publishing Ltd

Keywords: adaptive piezoelectric metamaterial, bandgap, broadband vibration attenuation, self-tuning impedance circuit, synthetic inductor, microcontroller

(Some figures may appear in colour only in the online journal)

## 1. Introduction

Low-frequency vibration has always plagued engineering applications, especially for the lightweight and precision structures widely utilized in modern aerospace/transportation industries [1]. The demand for new vibration control techniques has brought locally resonant metamaterial (metamaterial, for short) into focus. The local resonance bandgap in metamaterial allows wave attenuation in the sub-wavelength scale [2], far outperforming conventional vibration/noise control solutions. By considering elaborately manufactured resonators, including but not limited to mass-spring chains [3–7], mass-membrane resonators [8–10], Helmholtz resonators [11, 12], beam/plate-like resonators [13–15], a growing number of innovative designs for metamaterial have been proposed. The main limitation of these embodiments is the lack of tunability. In other words, the bandgap behavior and other physical characteristics are fixed once manufactured. Many researchers attempted to address this challenge by introducing reconfigurable/multistable structures into metamaterials. For instance, origami-type metamaterials [16–18] exhibit multiple stable states, and significant changes in physical properties are achieved through internal configuration switching. Except for origami, this concept has also been implemented by various bistable resonators [19, 20]. Nevertheless, the above solutions offer metamaterials only passive tunability, which depends on many factors, such as the excitation frequency and amplitude.

Piezoelectric metamaterials are raised by integrating periodic arrays of piezoelectric materials into host structures to achieve tunable bandgaps [21]. Analogous to mechanical resonators, the shunt circuits in piezoelectric metamaterials can be regarded as electromechanical resonators, and the electromechanical coupling-induced reaction force/moment leads to local resonance. On this basis, bandgaps can be flexibly controlled by changing external shunt circuits. Synthetic impedance circuits (also known as semi-active circuits) [22] generally consist of passive analog electronics and operational amplifiers (op-amps). They can emulate impedances beyond nominal values of common electronic elements, thus, are widely used in designing tunable piezoelectric metamaterials. In addition to tunability, more superior bandgap properties have also been achieved by using other synthetic impedance circuits, including broad bandgap [23–25], multiple bandgaps [26], and enhanced attenuation [27–29].

More recently, thanks to the advancement of digital control technology, digital synthetic impedance circuits (active circuits) have attracted extensive attention. Digital controllers are introduced in the shunts. Theoretically speaking, any arbitrary impedance can be emulated by the control law in the controller. This makes piezoelectric metamaterials more ‘smart’ and versatile by virtue of these advanced shunting strategies. Wang *et al* [30] experimentally validated the programable piezoelectric metamaterial using a microcontroller unit (MCU). The bandgap can be easily adjusted by purposefully configuring the poles and zeros of the transfer function coded into the controller. With a similar ‘pole-zero’ approach, Sugino *et al* [31] investigated the tunability of a digital piezoelectric metamaterial with shunt circuits implemented by a field-programmable gate array. In addition, piezoelectric metamaterials with cubic inductive [32] and nonlinear capacitive [33] circuitries achieved by digital synthetic impedance circuits have also been developed. For example, Zhang *et al* [33] proposed a piezoelectric metamaterial with nonlinear capacitor circuits. The construction of the nonlinear capacitor involves emulating the inverse nonlinear relationship between voltage and charge through digital controllers. The amplitude-dependent bandgap created in the nonlinear metamaterial provides a promising method to achieve broadband vibration suppression.

Overall speaking, the designs mentioned above allow the dynamic responses of metamaterials to be programmed online. Another significant merit of active shunt circuits is their potential to design adaptive bandgap behavior, which is beneficial to broaden the vibration attenuation region. Li *et al* [34] proposed a self-adaptive piezoelectric metamaterial using digitally controlled resonators. They carefully programmed the active shunt circuits connected to the piezoelectric elements (resonators). The effective stiffness of the resonator could adaptively change with the excitation frequency, leading to an attenuation region three times wider than its passive counterpart. Silva *et al* [35] investigated a piezoelectric metamaterial with self-tuning impedance circuits. An MCU was employed to detect the square wave type excitation signal and adjust the resonant circuit appropriately. An extra-broad attenuation region was experimentally confirmed. It should be mentioned that the above adaptive designs have a strict prerequisite that it is only applicable to harmonic excitations containing a single frequency, which greatly limits its application in complex vibration environments. Other experimental research related to self-tuning/adaptive piezoelectric metamaterials is very scarce.

In this paper, we present an adaptive piezoelectric metamaterial with shunt circuits realized by integrating synthetic impedance circuits and a digital controller for complex vibration scenarios. A theoretical framework for adaptive bandgap is provided, enabling the piezoelectric metamaterial’s dynamic response to frequency-varying harmonic vibrations and appropriately adjust when subjected to random vibrations. Experimental studies demonstrate that an ultra-broad vibration suppression is achieved for harmonic vibration. In addition, the self-adaptivity of the bandgap for white noise vibration with various spectra is experimentally validated.

The proposed adaptive metamaterial is significant for applying structural vibration attenuation in a real-world vibration environment. The paper is arranged as follows. Section 2 commences with designing adaptive strategies for the shunt circuit to handle multiple vibration types. The transfer matrix model of the piezoelectric metamaterial is also briefly introduced. One defect yet to be overcome in the model of piezoelectric metamaterial is pointed out in section 3, and a modified theoretical bandgap boundary expression is given. Based on the modified expression, section 4 presents experimental implementation of the control strategy and demonstrates the autonomous attenuation zone adjustment of the piezoelectric metamaterial under different types of vibration sources. Concluding remarks of this work are summarized in section 5.

## 2. Theoretical foundation

This section presents the concept of the adaptive piezoelectric metamaterial beam (piezo-meta-beam, for short). Focus is devoted to designing the self-tuning strategy for impedance circuits to allow the metamaterial system to respond adaptively to different types of vibrations with optimal attenuation. This section also briefly describes the dynamic model of the uniform piezo-meta-beam. The identification of the vibration sources and circuit implementation will be presented in section 4.

### 2.1. Piezoelectric metamaterial beam

The schematic diagram of the adaptive piezo-meta-beam system is shown in figure 1(a). The system comprises 9 cells ($S = 9$). The unit cell of the metamaterial beam is a composite beam consisting of a host beam and a pair of piezoelectric transducers (PZT is used in this work) with opposite polarization directions, as shown in the enlarged view in figure 1(b). The beam segment without PZT patches is denoted by $\alpha$, while the segment bonded with PZT patches is denoted by $\beta$. The geometry and material parameters of the unit cell are listed in table 1. Each pair of PZT patches is connected to a self-tuning impedance circuit (serial-wire operation). Note that the impedances of these circuits can be identical or different, and the value(s) are adaptively determined according to the vibration type. The cells are electrically independent, with a small gap $l_b$ between the adjacent PZT patches to ensure insulation. Base excitation is applied from one end of the beam. Only transverse motion is considered during the bending vibration.

### 2.2. Self-tuning strategy for impedance circuit

The mechanical/electrical properties of the piezoelectric transducer change significantly when electrical resonance occurs in the impedance circuit, forming the basis for opening the local resonant (LR) bandgap [36]. From the point of view of wave propagation, the bandgap refers to the frequency range for which there is no real wavenumber at a given frequency. Calculation of dispersion curves (i.e. wavenumber versus frequency) by band structure analysis gives a clear indication of the range of the bandgap. Since the vibration attenuation ability is attributed to the bandgap behavior, it is critical to fully understand the factors affecting the bandgap before designing the self-tuning strategy for the impedance circuit.

The three-dimensional (3D) constitutive equation of PZT can be written in the form of [37]

$$\begin{bmatrix} \mathbf{D} \\ \mathbf{S} \end{bmatrix} \begin{bmatrix} \varepsilon^T & \mathbf{d} \\ \mathbf{d}_t & \mathbf{s}^E \end{bmatrix} = \begin{bmatrix} \mathbf{E} \\ \mathbf{T} \end{bmatrix} \tag{1}$$

where **D, S, E, T** denote the tensorial representation of the electrical displacement, strain, electrical field, and stress, respectively. Equation (1) describes the coupling effect of the applied force load and electric fields on the strain and electrical displacements in PZT. Since only bending vibration is considered in this work, all surfaces on the PZT are assumed stress-free except for the 1 direction (material coordinate, in which 1 and 2 correspond to the plane direction $x$ and $y$, and 3 corresponds to the thickness direction $z$). Hence only the axis strain of PZT in 1 direction is considered. The 3D constitutive equation is simplified in the form of 1D, given by [38]

$$\begin{bmatrix} D_3 \\ S_1 \end{bmatrix} \begin{bmatrix} \varepsilon_{33}^T & d_{31} \\ d_{31} & s_{11}^E \end{bmatrix} = \begin{bmatrix} E_3 \\ T_1 \end{bmatrix} \tag{2}$$

where $d_{31}$ is the piezoelectric strain constant, $\varepsilon_{33}^{\mathrm{T}}$ is the permittivity component at constant strain, and $s_{11}^{\mathrm{E}}$ is the elastic compliance at a constant electric field. In the 1D model, It can be found that PZT is equivalent to a uniform material with in-plane Young's modulus $E_{\mathrm{p}}^{\mathrm{sc}} = 1/s_{11}^{\mathrm{E}}$.

Based on equation (2), the effective bending stiffness of the composite beam within a unit cell can be calculated. According to the bandgap generation mechanism, LR bandgaps appear when the effective stiffness is negative [36]. By letting the effective bending stiffness of a unit cell less than zero, the bandgap bound of a uniform piezo-meta-beam (i.e. the impedances in all shunt circuits are identical) can be derived as [39]:

$$\lambda_1 \omega_{LC} < \omega < \lambda_2 \omega_{LC} \tag{3}$$

where $\lambda_1 = \sqrt{1 - \frac{k_{31}^2}{1+\gamma}}$ and $\lambda_2 = \sqrt{1 - \frac{k_{31}^2}{1+\gamma/(1-\chi)}}$. $\omega_{LC} = 1/\sqrt{LC_{\mathrm{p}}^{\mathrm{S}}}$ is the resonance frequency of the $L$-$C$ oscillation, and $C_{\mathrm{p}}^{\mathrm{S}} = \varepsilon_{33}^{\mathrm{S}} b l_{\mathrm{p}}/(2h_{\mathrm{p}})$ denotes the internal capacitance of the PZT patch. $\varepsilon_{33}^{\mathrm{S}} = \varepsilon_{33}^{\mathrm{T}} - d_{31}^2/s_{11}^{\mathrm{E}}$ is the permittivity component at constant stress. $k_{31} = \sqrt{d_{31}^2/\left(s_{11}^{\mathrm{E}}\varepsilon_{33}^{\mathrm{T}}\right)}$ is the electromechanical coupling coefficient. $\gamma = \left(\left(1-k_{31}^2\right) E_{\mathrm{b}} b {h_{\mathrm{b}}}^3\right) / \left(E_{\mathrm{p}}^{\mathrm{sc}} b \left[(h_{\mathrm{b}} + 2h_{\mathrm{p}})^3 - {h_{\mathrm{b}}}^3\right]\right)$ denotes the ratio of the bending stiffness of the host beam to the PZT patch in the short circuit condition. $\chi = l_{\mathrm{p}}/(l_{\mathrm{b}} + l_{\mathrm{p}})$ is the coverage ratio of the PZT patch of one unit cell. From equation (3), it can be found that the bandgap location can be easily tuned by changing the resonance frequency $\omega_{LC}$. Hereafter, the tuning criterion for the impedance circuit is developed based on equation (3).

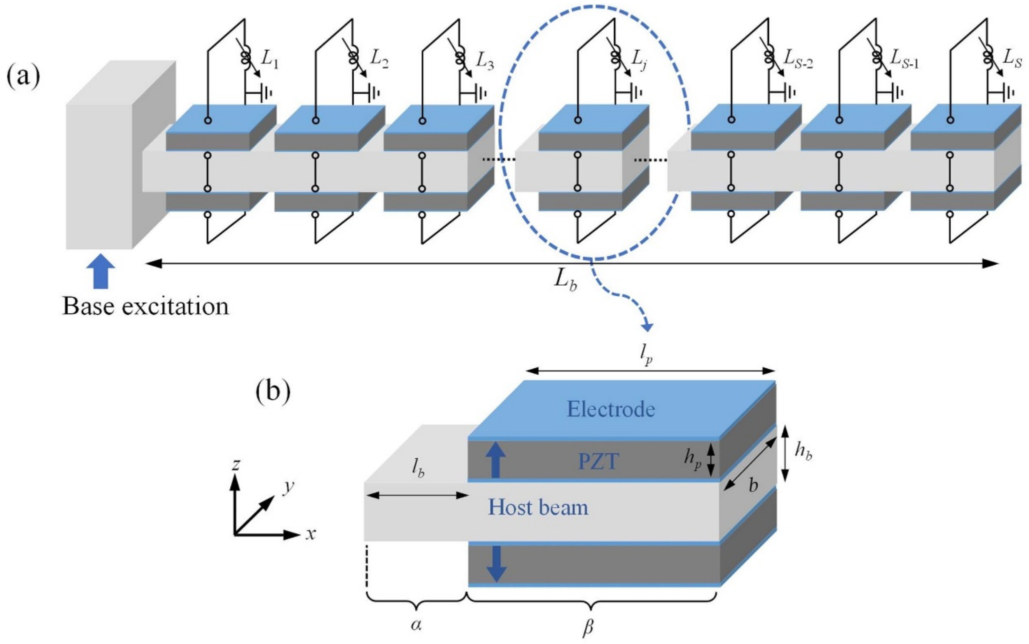

**Figure 1.** Schematic of the adaptive piezo-meta-beam: (a) a finitely long piezo-meta-beam with self-tuning impedance circuits; (b) illustration of a unit cell.

**Table 1.** Geometry and material properties of the piezo-meta-beam.

| Host beam | | PZT patch | |
|---|---|---|---|
| Material | Aluminum | Material | PZT-5H |
| Thickness $h_\mathrm{b}$ | 1 mm | Thickness $h_\mathrm{p}$ | 1 mm |
| Width $b$ | 30 mm | Width $b$ | 30 mm |
| Length $l_\mathrm{b}$ | 5 mm | Length $l_\mathrm{p}$ | 40 mm |
| Length $L_\mathrm{b}$ | 405 mm | Density $\rho_\mathrm{p}$ | 7500 kg m$^{-3}$ |
| Density $\rho_\mathrm{b}$ | 2700 kg m$^{-3}$ | Young's modulus in short-circuit condition $E_\mathrm{p}^\mathrm{sc}$ | 60.6 GPa |
| Young's modulus $E_\mathrm{b}$ | 69 GPa | Piezoelectric coefficient $e_{31}$ | $-16.61$ C m$^{-2}$ |
| | | Permittivity $\varepsilon_{33}^S$ | $2.5554 \times 10-^{08}$ F m$^{-1}$ |

To make the adaptive piezo-meta-beam applicable to the real environmental vibration, two typical vibration excitations are considered, namely, harmonic and band-limited white noise vibrations.

For harmonic vibration, the optimal design is straightforwardly to center the bandgap at the excitation angular frequency $\omega_h$. By combining with equation (3), the *L*-*C* resonance frequency $\omega_\mathrm{LC}$ should be tuned by:

$$\omega_{LC} = 2\omega_h / (\lambda_1 + \lambda_2) . \tag{4}$$

Note that $\omega_{LC}$ varies with the change of excitation frequency $\omega_h$.

For the band-limited white noise vibration, as a typical random vibration, its vibration energy remains constant over a certain spectrum. For brevity, this noise is described as ($\omega_\mathrm{c}$, $\Delta\Omega$), where $\omega_\mathrm{c}$ is the noise's central angular frequency, and $\Delta\Omega$ is the dominant spectrum. Two scenarios are considered. First, when $\Delta\Omega$ is narrower than the bandgap width, we can still center the bandgap to the center frequency of the noise. Similar to equation (4), we have

$$\omega_{LC} = 2\omega_\mathrm{c} / (\lambda_1 + \lambda_2) . \tag{5}$$

Second, when $\Delta\Omega$ is wider than the bandgap width, the attenuation capability of a piezo-meta-beam with identical impedance circuits is insufficient to counteract the excitation. To deal with it, the impedance circuits with gradually varying inductances can be designed to produce an array of 'graded' *L*-*C* resonance frequencies $\omega_{LC,j}$, $j = 1, 2,\ldots, S$. The metamaterial with this design is also known as 'graded metamaterial', which is regarded as a promising approach for broadband vibration suppression [40, 41]. Here, a first-order grading scheme [42] is adopted:

$$\omega_{LC,j} = \omega_{LC,m} + \Delta\omega - 2\Delta\omega \left( \frac{j-1}{S-1} \right) \tag{6}$$

where $\omega_{LC,j}$ denotes the resonance frequency of the *j*th impedance circuit. $\omega_{LC,m}$ corresponds to the resonance frequency of the circuit that is shunted to the middle PZT patches. $|2\Delta\omega|$ denotes the frequency spacing between the resonance frequencies of the 1st and *S*th circuits. The positive/negative $\Delta\omega$ corresponds to the descending/ascending order of the resonance frequency array $\omega_{LC,j}$. According to the conclusion drawn in [42], the descending mode exhibits better attenuation performance, which will be used in this work.

By combining equation (6) with equation (3), the bandgap bound of the piezo-meta-beam in the grading configuration is expanded to:

$$\lambda_1\left(\omega_{LC,m}-\Delta\omega\right)<\omega<\lambda_2\left(\omega_{LC,m}+\Delta\omega\right). \tag{7}$$

Similar to the previous cases, we locate the center of the bandgap to the center frequency $\omega_c$ of the noise:

$$\frac{\left(\lambda_1+\lambda_2\right)\omega_{LC,m}+\left(\lambda_2-\lambda_1\right)\Delta\omega}{2}=\omega_{\mathrm{c}}. \tag{8}$$

Obviously, when the bandgap width is wider than the dominant spectrum $\Delta\Omega$ of the noise, the excess attenuation region is unnecessary. Therefore, the bandgap width of the graded piezo-meta-beam is constrained to be equal to $\Delta\Omega$, yields:

$$\left(\lambda_2-\lambda_1\right)\omega_{LC,m}+\left(\lambda_1+\lambda_2\right)\Delta\omega=\Delta\Omega. \tag{9}$$

By simultaneously solving equations (8) and (9), $\omega_{LC,m}$ and $\Delta\omega$ can be calculated as:

$$\begin{aligned}\omega_{LC,m}&=\frac{2\left(\lambda_1+\lambda_2\right)\omega_c-\left(\lambda_2-\lambda_1\right)\Delta\Omega}{4\lambda_1\lambda_2};\\ \Delta\omega&=\frac{-2\left(\lambda_2-\lambda_1\right)\omega_c+\left(\lambda_1+\lambda_2\right)\Delta\Omega}{4\lambda_1\lambda_2}.\end{aligned} \tag{10}$$

Substituting equation (10) into equation (6) gives the resonance frequency of each impedance circuit:

$$\omega_{LC,j}=\kappa_1\omega_c+\kappa_2\Delta\Omega,\ j=\ 1,\ 2,\ldots,S \tag{11}$$

where $\kappa_1=\left[2\left(\lambda_1+\lambda_2\right)-2\left(\lambda_2-\lambda_1\right)\left(\frac{S-2j+1}{S-1}\right)\right]\Big/\left(4\lambda_1\lambda_2\right)$, $\kappa_2=\left[\left(\lambda_1+\lambda_2\right)\left(\frac{S-2j+1}{S-1}\right)-\lambda_2+\lambda_1\right]\Big/\left(4\lambda_1\lambda_2\right)$. Note that the designed $\omega_{LC,j}$ varies with the change of the center frequency $\omega_{\mathrm{c}}$ and dominant spectrum $\Delta\Omega$ of the noise excitation. By properly tuning the impedance circuits according to equations (4), (5) or (11), the piezo-meta-beam can adapt to different vibration sources.

### 2.3. Dynamic model with transfer matrix method (TMM)

Owing to the periodicity of the metamaterial, the frequency response characteristics of the piezo-meta-beam can be easily calculated by the TMM. The TMM model of a traditional uniform piezo-meta-beam has been extensively studied [43, 44]. Here, a brief introduction of the TMM model is given, and its results will be used as a reference during the discussion in section 3.

For the slender beam considered in this paper, the Euler–Bernoulli theory can be applied. The governing equation of the transverse motion $w(x,\ t)$ of the piezo-meta-beam can be written as

$$\frac{\partial^2}{\partial x^2}\left[D\left(x\right)\frac{\partial^2 w\left(x,t\right)}{\partial x^2}\right]+m\left(x\right)\frac{\partial^2 w\left(x,t\right)}{\partial t^2}=0 \tag{12}$$

where $D(x)$ and $m(x)$ are the flexural rigidity and the mass per unit length of the piezo-meta-beam, respectively. For the $j$th unit cell, $D(x)$ and $m(x)$ are in the form of

$$\begin{aligned}D\left(x\right)&=\begin{cases}D_\alpha=E_{\mathrm{b}}b{h_{\mathrm{b}}}^3/12,0\leqslant x<l_{\mathrm{b}}\\ D_\beta=E_{\mathrm{b}}b{h_{\mathrm{b}}}^3/12+E_{\mathrm{p}}\left(\omega\right)b\\ \qquad\times\left[\left(h_{\mathrm{b}}+2h_{\mathrm{p}}\right)^3-{h_{\mathrm{b}}}^3\right]/12,l_{\mathrm{b}}\leqslant x<l_{\mathrm{b}}+l_{\mathrm{p}}\end{cases}\\ m\left(x\right)&=\begin{cases}m_\alpha=\rho_{\mathrm{b}}bh_{\mathrm{b}},0\leqslant x<l_{\mathrm{b}}\\ m_\beta=\rho_{\mathrm{b}}bh_{\mathrm{b}}+2\rho_{\mathrm{p}}bh_{\mathrm{p}},l_{\mathrm{b}}\leqslant x<l_{\mathrm{b}}+l_{\mathrm{p}}\end{cases}\end{aligned}$$

where the equivalent Young's modulus of the $j$th PZT transducer when shunted to the impedance circuit $Z(\omega)$ is [45]

$$E_{\mathrm{p}}\left(\omega\right)=\frac{E_{\mathrm{p}}^{\mathrm{sc}}}{\left(1-k_{31}^2\right)}\left(1-\frac{k_{31}^2}{1+i\omega C_{\mathrm{p}}^{\mathrm{S}}Z\left(\omega\right)}\right). \tag{14}$$

The physical meanings of all symbols are given in table 1. The steady-state response of $w(x,\ t)$ in the $j$th unit cell is assumed to be

$$w\left(x,t\right)\ =W\left(x\right)e^{i\omega t}. \tag{15}$$

The general solution of the mode shape function $W(x)$ in the $j$th unit cell can be written as

$$W_{j,\ i}\left(x\right)=\mathbf{H}_i\mathbf{\Psi}_{j,\ i} \tag{16}$$

where $i=\alpha,\ \beta$. $\mathbf{H}_i=\left[\cos\left(k_ix\right),\sin\left(k_ix\right),\cosh\left(k_ix\right),\sinh\left(k_ix\right)\right]$ is the matrix with known parameters related to $x$. $\mathbf{\Psi}_{j,\ i}=\left[\bar{A}_{j,\ i},\bar{B}_{j,\ i},\bar{C}_{j,\ i},\bar{D}_{j,\ i}\right]^{\mathrm{T}}$ is the coefficient vector to be determined.

Considering the continuity conditions of the transverse displacement, angular displacement, bending moment, and shear force at the interface between segment ($j,\ \alpha$) and ($j,\ \beta$), and the continuity conditions at the interface between segment ($j$, $\beta$) and ($j$ + 1, $\alpha$), the transfer relationship between the $j$th and ($j$ + 1)th segment can be obtained as

$$\mathbf{\Psi}_{j+1,\alpha}=\mathbf{T}_j\mathbf{\Psi}_{j,\alpha} \tag{17}$$

where the transfer matrix is:

$$\mathbf{T}_j=\mathbf{H}_\alpha(0)^{-1}\mathbf{H}_\beta\left(l_p\right)\mathbf{H}_\beta(0)^{-1}\mathbf{H}_\alpha\left(l_{\mathrm{b}}\right). \tag{18}$$

By repeating the above procedures, the transfer relation between the left end of the 1st segment and the right end of the $S$th segment can be obtained as

$$\mathbf{\Psi}_{\mathrm{S},\beta}=\mathbf{H}_{\mathrm{S},\beta}(0)^{-1}\mathbf{H}_{\mathrm{S},\alpha}\left(l_{\mathrm{b}}\right)\left(\prod_{S-1}^{j=1}\mathbf{T}_j\right)\mathbf{\Psi}_{1,\alpha}. \tag{19}$$

Then, by considering a unit harmonic displacement $u_0(t)=e^{i\omega t}$ excitation is input from the clamped end and applying the clamped-free boundary condition to the piezo-meta-beam, the coefficient vector $\mathbf{\Psi}_{S,\beta}$ can be calculated. Thus, the transmittance of the piezo-meta-beam can be obtained as

$$\tau\left(\omega\right)=20\log_{10}\left|\mathbf{H}_{S,\beta}(l_p)_{1,:}\mathbf{\Psi}_{S,\beta}\right|\ (\mathrm{dB}) \tag{20}$$

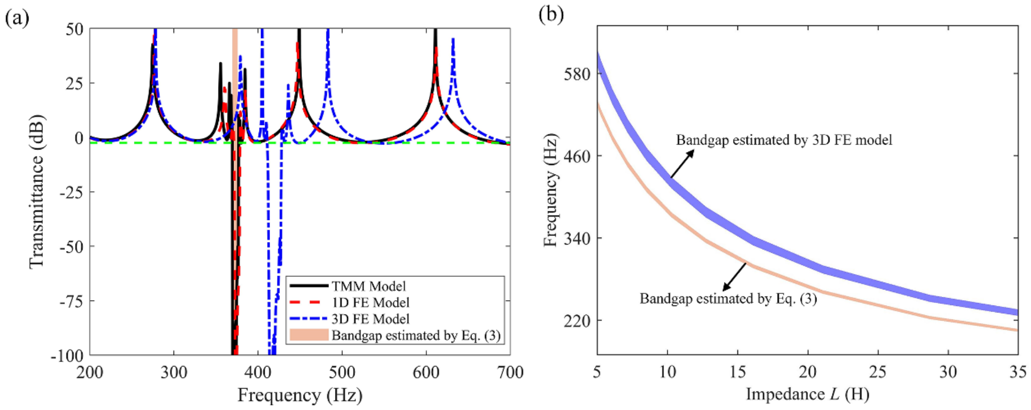

**Figure 2.** (a) Comparison of the transmittance responses of the uniform piezo-meta-beam calculated by TMM, 1D FE model, and 3D FE model. In addition, the bandgap estimated by equation (3) is shaded in orange for comparison; (b) the variation of the bandgaps obtained by the 3D FE model and equation (3) with the variation of impedance L.

where the subscript 1,: stands the 1st row of $\mathbf{H}_{S,\beta}(l_p)$. $\tau(\omega) < 0$ dB signifies a dampening of vibration. It is important to note that, due to the bandgap's definition based on an infinitely long structure, strictly speaking, the transmittance calculated from a finite-length structure can only approximately capture the bandgap. Fortunately, when a sufficient number of unit cells is present (generally exceeding six [38]), the bandgap range identified through the transmittance response closely aligns with that obtained from the dispersion relation. Hereafter, a lenient definition is employed to roughly pinpoint the bandgap range. Specifically, the bandgap is considered to be achieved when $\tau(\omega) < -2$ dB.

## 3. Issue in 1D piezoelectric constitutive equation and correction for bandgap

Since the self-tuning strategy highly depends on predicting the TBG,(for short), it is crucial to verify the accuracy of the TBG expression (i.e. equation (3)) first. The TBG expression was derived based on the simplified 1D piezoelectric constitutive equation. Although it has been widely used as a tuning criterion for many LR piezoelectric metamaterials [38, 46, 47], its verification through simulation/experiment is still lacking in the literature.

To this end, a corresponding finite element (FE) model of the uniform piezo-meta-beam is built in COMSOL Multiphysics to conduct a verification study. The default material properties of the piezoelectric material (PZT-5H adopted in this paper) in COMSOL are described by

$$\boldsymbol{\varepsilon}^S = \begin{bmatrix} \varepsilon_{11}^S & 0 & 0 \\ 0 & \varepsilon_{11}^S & 0 \\ 0 & 0 & \varepsilon_{33}^S \end{bmatrix}, \mathbf{d} = \begin{bmatrix} 0 & 0 & 0 & 0 & d_{15} & 0 \\ 0 & 0 & 0 & d_{15} & 0 & 0 \\ d_{31} & d_{31} & d_{33} & 0 & 0 & 0 \end{bmatrix}. \tag{21}$$

Since the PZT is polarized in the $z$-direction and electrodes are assumed to be perfectly conductive, there is no electric field in the 1 and 2 directions, implying $\varepsilon_{11}^S = 0$. Given the plane-stress assumption in the simplified 1D constitutive equation of the piezoelectric patch, the shear deformation and rotary inertia of the cross-section are neglected, implying that the shear and longitudinal modes-related piezoelectric coefficients, $d_{33} = d_{15} = 0$. Finally, the material properties of the PZT patch in COMSOL are modified to the form:

$$\boldsymbol{\varepsilon}^S = \begin{bmatrix} 0 & 0 & 0 \\ 0 & 0 & 0 \\ 0 & 0 & \varepsilon_{33}^S \end{bmatrix}, \mathbf{d} = \begin{bmatrix} 0 & 0 & 0 & 0 & 0 & 0 \\ 0 & 0 & 0 & 0 & 0 & 0 \\ d_{31} & d_{31} & 0 & 0 & 0 & 0 \end{bmatrix}. \tag{22}$$

For the convenience of distinction, the FE model of the piezo-meta-beam with default PZT's material properties is named the 3D FE model, while that with the modified properties is named the 1D FE model. As an example to show the difference between 1D and 3D FE models, we set the impedance $L = 10.3$ H (i.e. $LC$ resonance frequency $f_{LC} = 400$ Hz), and other parameters are the same as those in table 1. Figure 2(a) compares the tip transmittances of the uniform piezo-meta-beam calculated by the 1D and 3D FE models. The analytical results from the TMM model and the TBG estimated by equation (3) are also plotted in figure 2(a) for comparison. The dashed green line corresponds to $\tau(\omega) = -2$ dB is plotted in figure 2(a) as a reference. Note that the transmittance where $\tau(\omega) < -2$ dB(i.e. the valley) indicates the bandgap. It is observed that the 1D FE model is in good agreement with the TMM model. In addition, the TBG by equation (3) (orange area) also matches the bandgap (i.e. the valley of the transmittance) predicted by the TMM and 1D FE models.

However, it is noted that the bandgap region in the transmittance of the 3D FE model shifts to a 12% higher frequency and becomes 129% wider. This phenomenon was also noted in a previous experiment [35] and attributed it to the variation of component parameters in actual shunt circuits. However, the parameters of the impedance circuits in this FE simulation are ideal, which means there is no circuit parameter error. Figure 2(b) compares the variation of the TBG and the bandgap calculated by the 3D FE model when the impedance of the shunt circuit varies. It is noted that the bandgap calculated by the 3D FE model is always above and broader than the TBG. The potential reason might be that the estimated

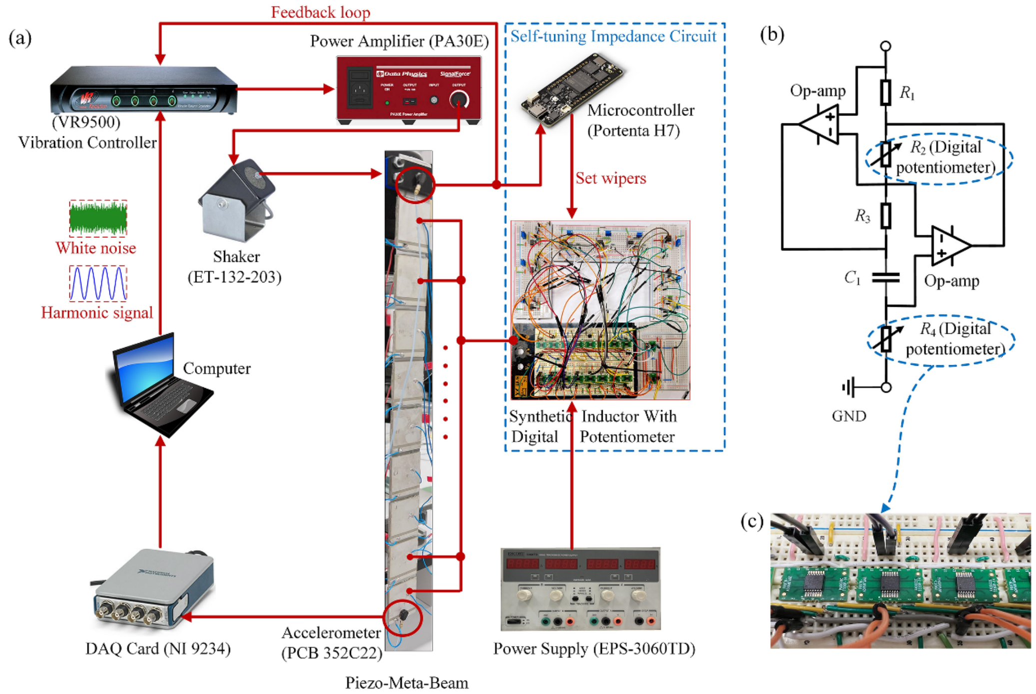

**Figure 3.** (a) Experimental setup for testing the adaptive piezo-meta-beam; (b) circuit diagram of the synthetic inductor; (c) illustration of the digital potentiometers controlled by the microcontroller.

piezoelectric patch's capacitance $C_p^S$ based on the 1D piezoelectric constitutive equation is under the assumption of a fully clamped constraint. However, the actual capacitance of a piezoelectric patch is affected by its boundary conditions. For the piezoelectric patches glued on the clamped-free piezo-meta-beam, their capacitance values should be smaller than $C_p^S$ since they are loosely constrained. In this case, the piezoelectric patch in the 3D FE model is considered as a more accurate representation of the actual piezoelectric patch, which is why the 3D FE model always exhibits higher bandgap frequencies. However, it should be emphasized that variations in capacitance may be only one of the main factors contributing to the bandgap discrepancy. Different boundary conditions arising from the simplified 1D piezoelectric constitutive equations will also change the piezoelectric coupling strength, which in turn affects the bandgap. In addition, other factors, such as the drift of synthetic inductance and the temperature of transducers, will also affect the bandgap range in practical applications.

To match the bandgap estimated by the 3D FE model, a correction is made for equation (3) as

$$\bar{\lambda}_1 \omega_{LC} < \omega < \bar{\lambda}_2 \omega_{LC} \tag{23}$$

where $\bar{\lambda}_1 = 1.1115\sqrt{1 - \frac{k_{31}^2}{1+\gamma}}$ and $\bar{\lambda}_2 = 1.1363\sqrt{1 - \frac{k_{31}^2}{1+\gamma/(1-\chi)}}$. The modified theoretical bandgap is named MTBG. The parameters in the tuning criterion (equation (4), (5) and (11)) are, thereby, updated accordingly. It should be pointed out that using experimental results to correct the TBG or discarding the TBG and using experimentally based numerical bandgaps to guide the bandgap design are both relatively simple approaches. However, the use of the 3D FE model to correct TBG is more versatile, especially for some studies that lack experiments.

## 4. Experiment

### 4.1. Experimental setup

A series of experiments are carried out to validate the adaptive vibration suppression capability of the proposed piezo-meta-beam system when subjected to different types of vibration sources. A piezo-meta-beam made of an aluminum host beam and 9 bimorph piezoelectric elements (PZT-5H) was fabricated and clamped vertically, as shown in figure 3(a). The internal capacitance $C_p^{\mathrm{exp}}$ of the PZT patches was measured to be 15.6 nF. Electrically insulative epoxy was used to glue the PZT patch to the aluminum beam. Details on the geometric and material parameters used for this prototype have been given in table 1. The clamped end of the piezo-meta-beam is fixed to the armature of an electromagnetic shaker. Acceleration responses at the excitation and free-end points of the beam are acquired by the attached accelerometers. An overview of the experimental setup is shown in figure 3(a). The self-tuning impedance circuits, presented in the blue dashed box in figure 3(a), were implemented by synthetic inductors and a microcontroller. The advantage of the synthetic inductor over the bulky passive inductor lies in the smaller additional mass and internal resistance. The circuit diagram of the synthetic inductor is

**Table 2.** Resistance value of $R_2$ for different frequency ranges of excitation.

| | 200 ~ 240 Hz | 240 ~ 320 Hz | 320 ~ 400 Hz | 400 ~ 560 Hz | 560 ~ 700 Hz |
|---|---|---|---|---|---|
| $R_2$ | 1100 Ω | 1400 Ω | 2400 Ω | 4000 Ω | 4500 Ω |

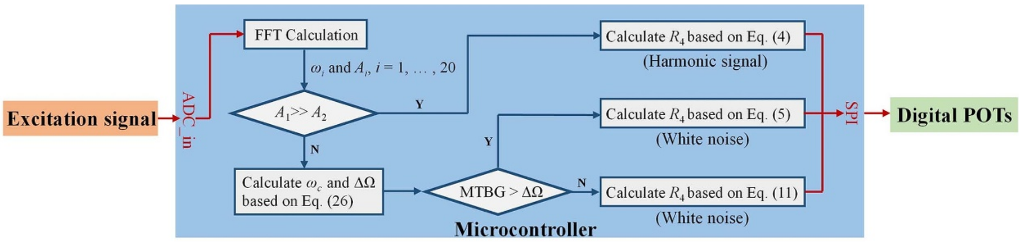

**Figure 4.** Global architecture of the self-tuning impedance circuit.

shown in figure 3(b). The equivalent impedance of the synthetic inductor can be calculated by [48]

$$L = \frac{R_1 R_3 R_4}{R_2} C_1. \tag{24}$$

In the experiment, $R_1 = R_3 = 10$ kΩ, and $C_1 = 100$ nF are used. The type of op-amp is LM358. To achieve impedance self-tuning, the digital potentiometer (POT) (MCP41HV31-502) ranging from 0 ~ 5 kΩ is utilized for $R_4$, as shown in figure 3(c).

Through SPI serial interface, the resistance value of the digital POT can be controlled by the microcontroller, as given by

$$R_4 = \frac{R_2 \omega_{LC}^2}{R_1 R_3 C_1 C_{\mathrm{p}}^{\mathrm{exp}}} \tag{25}$$

where $\omega_{LC}$ is the target *L*-*C* resonance frequency of each shunt circuit, which is calculated by equations (4), (5) or (11). The tuning strategy selection depends on the detected excitation type and is conducted by the microcontroller. The digital POT used has a 7-bit encoding ability, implying a resolution of 5000/128 Ω. The POT's resolution is critical because it directly determines the minimum frequency spacing when adjusting the bandgap. In addition, as shown in figure 2(b), the bandgap variation in higher frequency is more sensitive to the impedance change. Therefore, the digital POT's one-step adjustment will more easily cause an undesirable change in bandgap location at high frequency. To minimize the bandgap location variation when $R_4$ changes, $R_2$ in the synthetic inductor circuits is also implemented by a digital POT, whose value is carefully designed for the interested frequency range of excitation, as given in table 2. In summary, a total of 2 × 9 digital POTs are used. The 9 digital POTs for constituting $R_4$ are controlled independently, while the other 9 digital POTs for making up $R_2$ share the same command pins. A high-performance commercial development board (Portenta H7) is employed to control the digital POTs and detect the excitation frequency. This microcontroller is configured with 15 DAC channels of up to 16-bit to guarantee the requirements of digital POT control.

For the part of tuning strategy selection, the harmonic or white noise excitation signal is fed into the ADC channel of the microcontroller. The frequency components and the corresponding amplitudes are calculated in real-time by the Fast Fourier Transform (FFT) inside the microcontroller. The first $n$ frequency components ($\omega_i$, $i = 1, 2, \ldots, n$) with the largest amplitude $A_i$ are extracted in descending order of their amplitudes. Generally, the excitation is a harmonic signal if the amplitude of the first frequency component is much larger than others, i.e. $A_1 \gg A_2$. In contrast, the excitation will be assessed as white noise if multiple comparable frequency components evenly distribute over a certain spectrum, e.g. $A_1 \approx A_2$. Therefore, the discrepancy between $A_1$ and $A_2$ is used as a criterion to distinguish the excitation types. Subsequently, according to the identified excitation, different tuning strategies will be chosen to determine the digital POT's value to make the shunt circuit adaptable. Moreover, in the case of white noise, additional required values, i.e. the center frequency $\omega_c$ and the dominant spectrum $\Delta\Omega$ are calculated by:

$$\omega_c = \frac{1}{n} \sum_{i=1}^{n} \omega_i, \; \Delta\Omega = \max(\omega_i) - \min(\omega_i). \tag{26}$$

The global architecture of the self-tuning impedance circuit is shown in figure 4.

It is worth mentioning that the accuracy of the excitation frequency calculated by FFT depends on the sampling number *N*. However, a large *N* requires large memory in the microcontroller. Fortunately, the Portenta H7 commercial board has up to 8 Mbytes of RAM, and the embedded STM32H747 processor has a clock speed of 480 MHz, which can ensure the implementation of high-point FFT and fast response to the excitation signal. In the experiments, the number of samples is set to $N = 2^{15}$ and $n = 60$ (i.e. the first 60 frequency components are extracted). Tests on harmonic signals show that

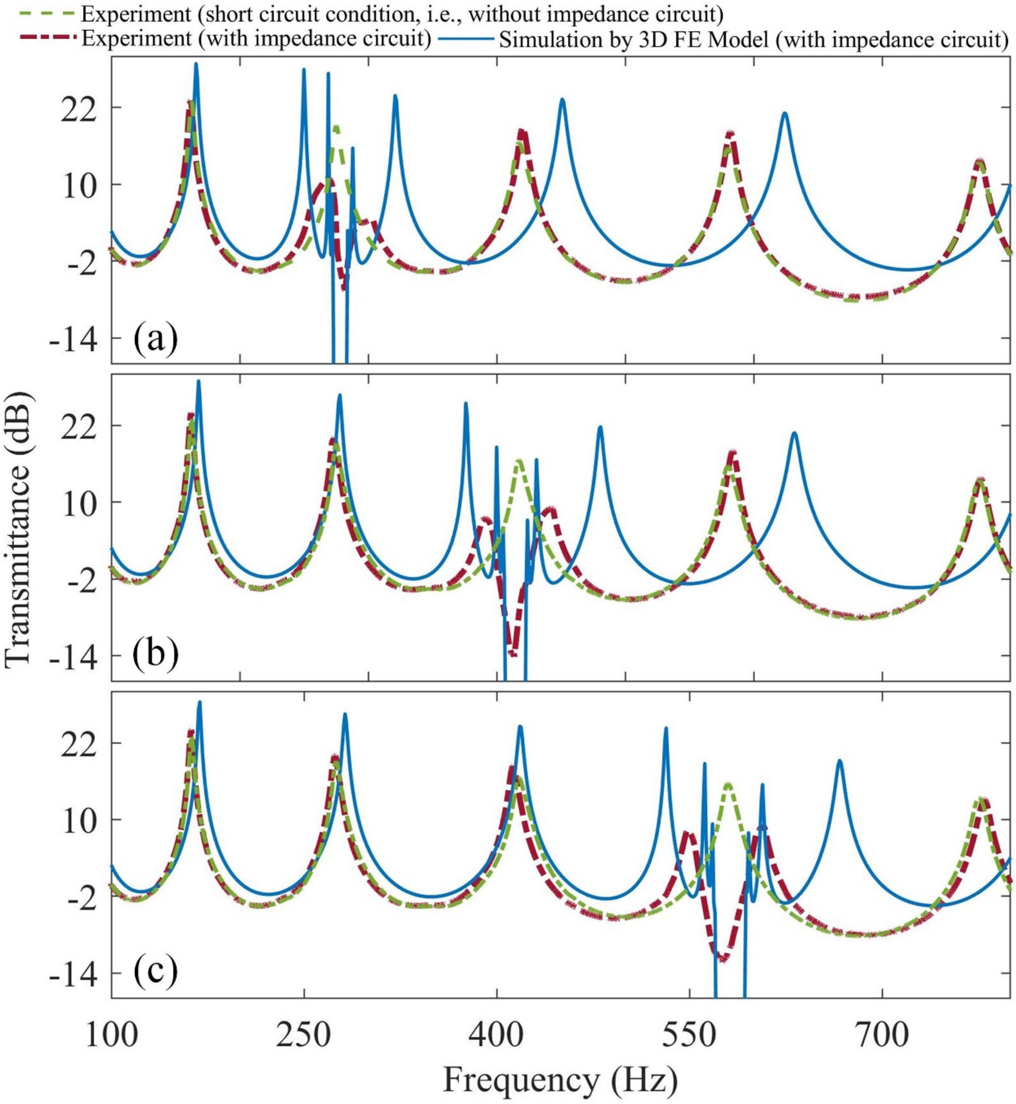

**Figure 5.** Comparison between the transmittances of the uniform piezo-meta-beam with the synthetic inductor impedance circuits from the experiment and 3D FE model: (a) L = 24.2 H; (b) L =10.4 H; (c) L = 5.4 H. The measured transmittance of the uniform piezo-meta-beam when all the impedance circuits are short-circuited is also plotted as a reference.

the FFT process takes a computation time of around 600 ms, with a relative error of 0.05%.

### *4.2. Results and discussion*

*4.2.1. Validation of 3D FE model.* Firstly, we validate the 3D FE model of the piezo-meta-beam. The self-tuning feature in the synthetic inductor circuit is momentarily disabled. Digital POTs having identical resistances are set manually. In other words, the adaptive piezo-meta-beam degenerated into a conventional uniform piezo-meta-beam. Figure 5 compares the experimentally measured transmittance responses of the uniform piezo-meta-beam with the results from the 3D FE simulation. Three inductances $L$, i.e. $L = 24.2$ H, $L = 10.4$ H, and $L = 5.4$ H, are considered to make the piezo-meta-beam generate bandgaps around its modal peaks. It is observed that the measured bandgap locations generally agree with those calculated by the 3D FE model, albeit the intensity of the measured attenuation regions is weaker than the simulational predictions. The weaker attenuation performance in practice is unavoidable, and many factors could be responsible for it. The two most possible reasons are: (1) The PZT patches are not perfectly glued on the host beam. The epoxy layer leads to a weak electromechanical coupling between PZT and the beam and introduces large damping at the same time; (2) The electrical damping induced by the parasitic resistance in the real synthetic circuit.

It is also found that the measured frequency response differs from that of the 3D FE model, and this difference becomes more pronounced at high frequencies. Various factors may contribute to this discrepancy, including the relatively loose clamping condition in the prototype, the variation in the mass

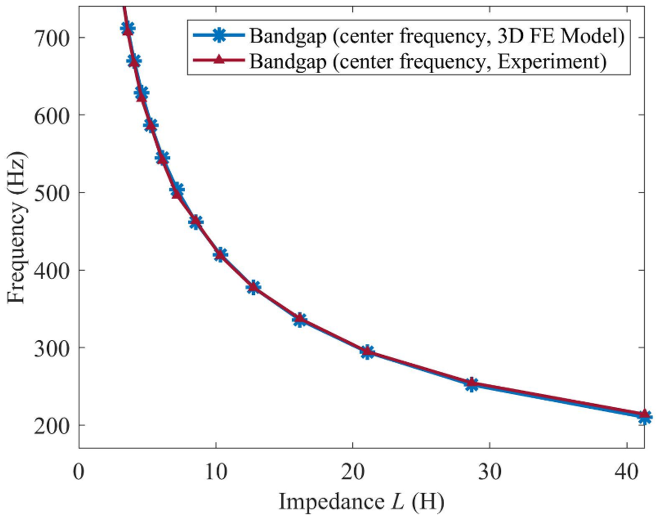

**Figure 6.** Variation of the center frequency of bandgap with the change of impedance $L$. Note that the blue line represents that from the prediction of the 3D FE model, and the purple line represents that from the experimental measurement.

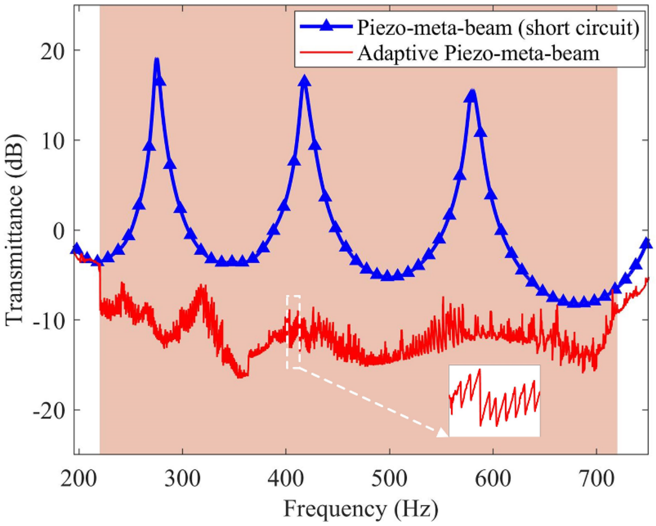

**Figure 7.** The experimentally measured transmittance response of the adaptive piezo-meta-beam when subjected to a harmonic sweep excitation with the sweeping rate of 2 Hz $s^{-1}$. The transmittance of the piezo-meta-beam in the short circuit condition is also shown for reference.

of the host beam caused by the uneven distribution of density, and the additional mass introduced by the epoxy layer. Note that for vibrating systems, in general, the effect of changes in mass on the frequency response becomes more significant as the frequency increases [49]. A possible improvement is to conduct parametric identifications for the piezoelectric metamaterial beam in the short/open circuit condition. Similar studies can be found in [50, 51]. The 3D FE model is then tuned according to the experimentally identified results. This is expected to improve the accuracy of the FE model in estimating the frequency response beyond the bandgap. However, from figure 5, it is evident that the 3D FE model provides a sufficiently accurate bandgap estimation, which is enough to realize the focus of this study, i.e., the automatic tuning of the bandgap. The work on parameter identification can be left for future improvement.

For several more validation cases, figure 6 compares the center frequencies of the bandgap obtained by the 3D FE model and experiment. It can be seen that the bandgap locations obtained by the two ways are generally consistent (maximum relative error in the range of interest: 1.7%), implying that the error of MTBG (i.e. equation (23)) is within the accepted range and the tuning strategies based on MTBG are reliable. To the authors' best knowledge, this is the first experimental validation for the bandgap location of the uniform piezo-meta-beam. It is also found that the bandgap of the conventional piezo-meta-beam is narrow, with a width of only 10 Hz–20 Hz. Hereafter, the self-tuning strategy in the shunt circuit is activated, and the adaptive behavior of the piezo-meta-beam is studied under different excitations.

### 4.2.2. Autonomous tuning under harmonic sweep excitation.

To investigate the performance of the adaptive piezo-meta-beam under harmonic excitation, a harmonic sweep excitation with a sweeping rate of 2 Hz $s^{-1}$ is exerted on the clamp end of the piezo-meta-beam. According to the FFT analysis in the control unit, the harmonic wave-related tuning strategy will be automatically selected. Figure 7 shows the transmittance response of the adaptive piezo-meta-beam. As a reference, the transmittance of the piezo-meta-beam when all shunt circuits are shorted is also plotted in figure 7. It can be seen that the original three modal peaks of the piezo-meta-beam are suppressed with an ultra-broad attenuation zone achieved, as shaded in orange ranging from 220 to 720 Hz (bandwidth of 500 Hz). It should be pointed out that the wide attenuation zone is not a bandgap. Precisely, it is produced by the automatic adjustment of the original narrow bandgap of

**Table 3.** Predefined spectra of the white noise excitation used in the studied cases.

| | Case 1 | Case 2 | Case 3 | Case 4 | Case 5 | Case 6 |
|---|---|---|---|---|---|---|
| Center frequency $f_\mathrm{c}$ | 275 Hz | 418 Hz | 580 Hz | 580 Hz | 580 Hz | 580 Hz |
| Dominant spectrum $\Delta f$ | 10 Hz | 14 Hz | 20 Hz | 60 Hz | 80 Hz | 160 Hz |

the uniform piezo-meta-beam as the excitation frequency varies. One can observe that the attenuation profile is not flat. This is because of the tiny difference between MTBG and the measured bandgap, resulting in the center of the bandgap adjusted based on equation (4) not being perfectly aligned with the excitation frequency. The enlarged view of the attenuation region in figure 7 further displays the adjustment of the narrow bandgap, in which the sawtooth-like curve is due to the overlap of the bandgap in one adjustment. Recall that the adjustment frequency relies on the digital POT's resolution, and the higher this frequency, the more accurate the bandgap repositioning.

*4.2.3. Autonomous tuning under band-limited noise excitation.* The harmonic vibration can be regarded as a particular limit case of environmental vibration. Aiming to meticulously test the adaptive vibration suppression capacity of the piezo-meta-beam under random vibration conditions, we designed six white noise excitation cases with different spectra, as summarized in table 3.

The predefined white noise excitation can be generated by the vibration controller VR9500, and the power spectral density (PSD) of the excitation for all six cases is set to 0.001 $\mathrm{G}^2\ \mathrm{Hz}^{-1}$, where G stands for gravitational acceleration. In cases 1–3, multiple frequency components are detected by the FFT computation in the control unit. Based on equation (26), the calculated center frequencies are 273.6 Hz, 421.3 Hz, and 578.1 Hz, respectively. The calculated dominant spectrums are 10.2 Hz, 12.8 Hz, and 18.6 Hz, respectively, which are narrower than the associated MTBG (i.e. 11.2 Hz, 17.0 Hz, 23.6 Hz, respectively). Therefore, the control unit will choose the white noise-related tuning criterion (equation (5)) in accordance with the algorithmic procedure shown in figure 4. Results for cases 1–3 are depicted in row (I–III) of figure 8, correspondingly. Column (a) in figure 8 displays the acceleration signal at the beam tip of the adaptive piezo-meta-beam during 30 s of excitation. A large acceleration can be observed in the initial phase. A significant drop in acceleration afterward indicated that the bandgap had been properly tuned after a short period of FFT calculation and digital POT setting. Column (b) in figure 8 further compares the PSD at the beam tip before and after bandgap tuning. As can be seen, once the bandgap is adaptively tuned, the PSD in the frequency range of the noise excitation is significantly reduced. Additionally, to quantify the time domain results, the root-mean-square (RMS) values of the tip acceleration signal are calculated and shown in column (c) in figure 8. The acceleration signals related to the marked RMS values are superimposed on the column plot (c). It is observed that for cases 1–3, the RMS accelerations are maintained at a very low value (<0.1 G) after adaptively tuning. In summary, the studies in cases 1–3 demonstrate that the adaptive piezo-meta-beam can effectively handle the noise excitation with a narrower dominant spectrum than the MTBG.

In cases 4–6, the detected dominant spectrums (i.e. 63.5 Hz, 78.4 Hz, and 157.7 Hz, respectively) by the FFT computation are broader than the MTBG at the corresponding center frequency. According to the algorithmic procedure shown in figure 4, the microcontroller will implement the tuning criterion equation (11), to achieve the 'graded' synthetic inductors design. Results for cases 4–6 are, respectively, depicted in row (I–III) of figure 9. From figures 9(I-a) and (II-a), one can still see an apparent decrease in the acceleration signal.

However, for the noise excitation with a 160 Hz dominant spectrum (case 6), the vibration suppression is relatively inappreciable, as shown in figure 9(III-a). The reason can be found in the PSD analysis in figure 9(b). The PSD curves after tuning in figures 9(I-b) and (II-b) display clear vibration attenuation regions (i.e. valleys) that encompass the frequency range of the associated noise excitation (i.e. 550–610 Hz, 540–620 Hz, respectively), which confirms that the original narrow bandgap is expanded after adopting the grading design-based tuning strategy. However, the attenuation region in the after-tuning PSD curve of figure 9(III-b) does not cover the frequency range of the noise excitation (500–660 Hz). Recall that the tuning strategy of equation (11) depends on the dominant frequency $\Delta f$, while the width $\Delta f = 160$ Hz drives a large frequency spacing of the $L$-$C$ resonance frequency array $\omega_{LC,j}$, resulting in over-tuning of the graded inductance. According to the result reached in [40], the over-tuning of the graded metamaterial may cause the vibration attenuation regions to be too dispersed in the frequency spectrum or even disappear. As a result, a limitation of the adaptive piezo-meta-beam is its difficulty in dealing with noise excitations with broad dominant spectra. Hence, figure 9(III) presents an example of an over-tuned case. In addition, the RMS acceleration histories of the tip acceleration signal for cases 4–6 are given in column (c) in figure 9. Again, the poorest performance is observed in figure 9(III-c). In particular, the subplot of the acceleration signal corresponding to the green marker points shows that there is almost no attenuation effect for certain frequency components. It should be noted that metamaterials exhibit sensitivity to random vibrations, necessitating the use of a very accurate model to precisely predict random vibration responses and prevent significant errors. However, as previously mentioned,

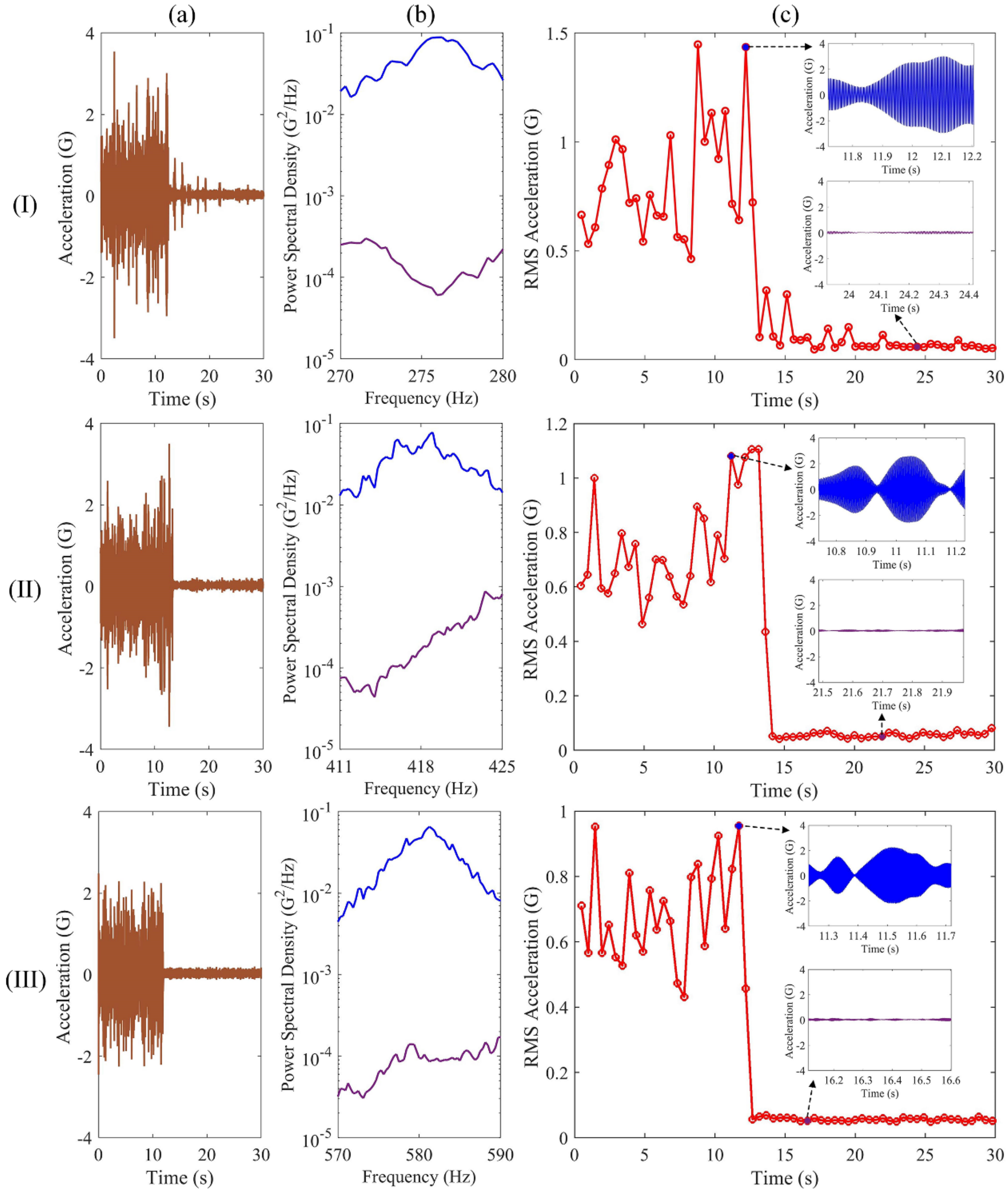

**Figure 8.** Rows (I) to (III) respectively plot the results when the noise excitations of cases 1–3 are applied. Column (a) presents the time-domain acceleration signal at the tip end of the adaptive piezo-meta-beam during 30 s of excitation. Column (b) compares the PSD at the tip of the adaptive piezo-meta-beam before (blue line) and after (purple line) the adaptive adjustment of the bandgap. Column (c) presents the evolution of the RMS accelerations at the tip of the adaptive piezo-meta-beam. In addition, the slices of the time domain signals corresponding to the marked RMS value are superposed on the plots in column (c).

existing models based on the 1D piezoelectric constitutive equation exhibit notable limitations, and a highly accurate model for piezoelectric metamaterials is not yet built in the literature. Therefore, the future pursuit of random vibration studies needs to incorporate the random vibration theory and consider the 3D piezoelectric constitutive equations in the theoretical model, thus paving the way for improved suppression strategies for dealing with random excitations.

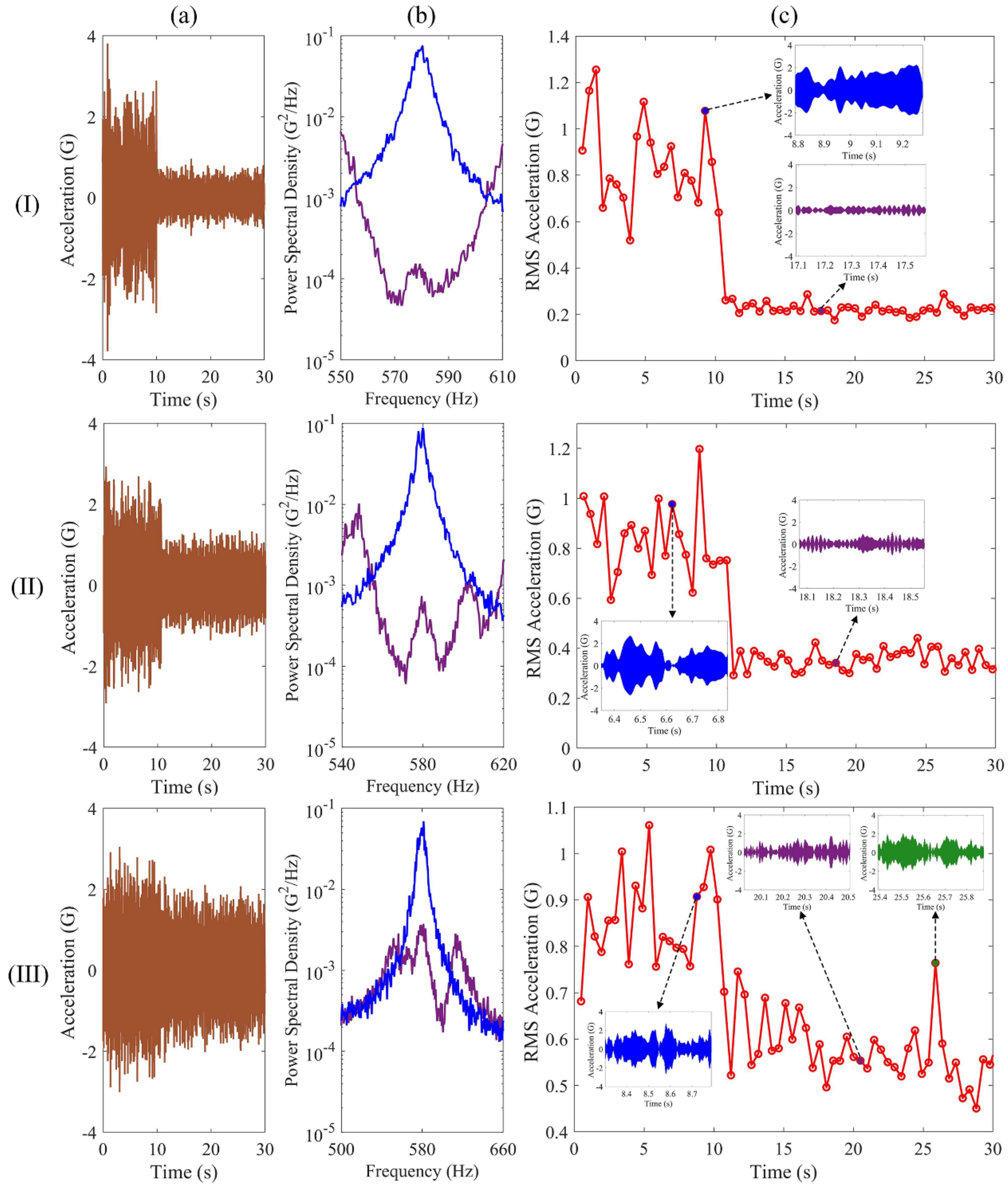

**Figure 9.** Rows (I) to (III) respectively plot the results when the noise excitations of cases 4–6 are applied. Column (a) presents the time-domain acceleration signal at the tip end of the adaptive piezo-meta-beam during 30 s of excitation. Column (b) compares the PSD at the tip end of the adaptive piezo-meta-beam before (blue line) and after (purple line) the adaptive adjustment. Column (c) presents the evolution of the RMS accelerations at the tip of the adaptive piezo-meta-beam. In addition, the slices of the time domain signals corresponding to the marked RMS value are superposed on the plots in column (c).

## 5. Conclusions

This paper has proposed an adaptive piezoelectric metamaterial beam (piezo-meta-beam) with self-tuning impedance circuits. It can automatically adjust its dynamic response when subjected to different types of excitations. Two bandgap tuning strategies are designed to handle two typical vibration scenarios: harmonic vibration and white noise vibration over a certain dominating spectrum. The key concept of the self-tuning impedance circuit is to replace physical resistors with microcontroller-driven digital POTs in the synthetic inductor circuits. A control architecture based on designed tuning strategies is developed and executed by a microcontroller. The vibration type is also identified by an algorithm based on the FFT analysis processed by the microcontroller. The tuning strategies are based on matching the band gap with the detected excitation frequency. Therefore, band gap prediction accuracy directly determines the robustness of tuning strategies. The bandgap boundary expression (TBG) was first revisited and verified by comparing the TMM, 1D FE, and 3D FE models. A significant discrepancy in the TBG was noticed. A modified bandgap boundary expression (MTBG) was then proposed. The MTBG results agreed well with the experimental results. An adaptive piezo-meta-beam prototype was fabricated and experimentally tested. For the harmonic excitation, it was found that the bandgap was smoothly tuned autonomously when the excitation frequency varied, leading to an ultra-broad attenuation bandwidth (220–720 Hz) that could cover three intrinsic resonant peaks of the piezo-meta-beam. For the white noise excitation, we also validated that the bandgap adaptively adjusted according to the identified excitation spectra, allowing the attenuation zone to cover the dominating noise excitation spectrum. Generally speaking, the proposed piezo-meta-beam exhibited high flexibility and intelligence in coping with realistic and complex vibration scenarios.

## Data availability statement

All data that support the findings of this study are included within the article (and any supplementary files).

## Acknowledgments

This work was financially supported by a PhD scholarship from the China Scholarship Council (No. 201907000126) and the International Innovation Cooperation Project Supported by Sichuan Science and Technology Program (Contract No. 2020YFH0066).

## ORCID iDs

Guobiao Hu https://orcid.org/0000-0002-1288-7564
Lihua Tang https://orcid.org/0000-0001-9031-4190

## References

[1] Li C, Jiang T, He Q and Peng Z 2020 Stiffness-mass-coding metamaterial with broadband tunability for low-frequency vibration isolation *J. Sound Vib.* **489** 115685

[2] Liu Y, Jin L, Wang H, Liu D and Liang Y 2021 Topological interface states in translational metamaterials for sub-wavelength in-plane waves *Int. J. Mech. Sci.* **197** 106308

[3] He F, Shi Z, Qian D, Tu J and Chen M 2022 Flexural wave bandgap properties in metamaterial dual-beam structure *Phys. Lett.* A **429** 127950

[4] Wu Z, Liu W, Li F and Zhang C 2019 Band-gap property of a novel elastic metamaterial beam with X-shaped local resonators *Mech. Syst. Signal Process.* **134** 106357

[5] Pai P F, Peng H and Jiang S 2014 Acoustic metamaterial beams based on multi-frequency vibration absorbers *Int. J. Mech. Sci.* **79** 195–205

[6] Bao H, Wu C, Wang K and Yan B 2021 An enhanced dual-resonator metamaterial beam for low-frequency vibration suppression *J. Appl. Phys.* **129** 095106

[7] Jian Y, Hu G, Tang L, Xu J and Aw K C 2021 A generic theoretical approach for estimating bandgap bounds of metamaterial beams *J. Appl. Phys.* **130** 054501

[8] Gao C, Halim D and Yi X 2020 Study of bandgap property of a bilayer membrane-type metamaterial applied on a thin plate *Int. J. Mech. Sci.* **184** 105708

[9] Chen J-S, Huang Y-J and Chien I-T 2017 Flexural wave propagation in metamaterial beams containing membrane-mass structures *Int. J. Mech. Sci.* **131** 500–6

[10] Lu Z, Yu X, Lau S-K, Khoo B C and Cui F 2020 Membrane-type acoustic metamaterial with eccentric masses for broadband sound isolation *Appl. Acoust.* **157** 107003

[11] Hu G, Tang L and Cui X 2019 On the modelling of membrane-coupled Helmholtz resonator and its application in acoustic metamaterial system *Mech. Syst. Signal Process.* **132** 595–608

[12] Dogra S and Gupta A 2021 Design, manufacturing, and acoustical analysis of a helmholtz resonator-based metamaterial plate *Acoustics* **3** 630–41

[13] Fan X, Li J, Zhang X and Li F 2022 Multi-bandgaps metamaterial plate design using complex mass-beam resonator *Int. J. Mech. Sci.* **236** 107742

[14] Jung J, Goo S and Wang S 2020 Investigation of flexural wave band gaps in a locally resonant metamaterial with plate-like resonators *Wave Motion* **93** 102492

[15] El-Borgi S, Fernandes R, Rajendran P, Yazbeck R, Boyd J and Lagoudas D 2020 Multiple bandgap formation in a locally resonant linear metamaterial beam: theory and experiments *J. Sound Vib.* **488** 115647

[16] Silverberg J L, Evans A A, McLeod L, Hayward R C, Hull T, Santangelo C D and Cohen I 2014 Using origami design principles to fold reprogrammable mechanical metamaterials *Science* **345** 647–50

[17] Ji J, Luo Q and Ye K 2021 Vibration control based metamaterials and origami structures: a state-of-the-art review *Mech. Syst. Signal Process.* **161** 107945

[18] Zhang M, Yang J and Zhu R 2021 Origami-based bistable metastructures for low-frequency vibration control *J. Appl. Mech.* **88** 051009

[19] Meaud J and Che K 2017 Tuning elastic wave propagation in multistable architected materials *Int. J. Solids Struct.* **122** 69–80

[20] Frazier M J and Kochmann D M 2017 Band gap transmission in periodic bistable mechanical systems *J. Sound Vib.* **388** 315–26

[21] Xu J and Tang J 2017 Tunable prism based on piezoelectric metamaterial for acoustic beam steering *Appl. Phys. Lett.* **110** 181902

[22] Fleming A, Behrens S and Moheimani S 2000 Synthetic impedance for implementation of piezoelectric shunt-damping circuits *Electron. Lett.* **36** 1

[23] Yi K and Collet M 2021 Broadening low-frequency bandgaps in locally resonant piezoelectric metamaterials by negative capacitance *J. Sound Vib.* **493** 115837

[24] Chen S-B, Wen J-H, D-L Y, Wang G and Wen X-S 2011 Band gap control of phononic beam with negative capacitance piezoelectric shunt *Chin. Phys.* B **20** 014301

[25] Zhang H, Wen J, Xiao Y, Wang G and Wen X 2015 Sound transmission loss of metamaterial thin plates with periodic subwavelength arrays of shunted piezoelectric patches *J. Sound Vib.* **343** 104–20

[26] Zhou W, Wu Y and Zuo L 2015 Vibration and wave propagation attenuation for metamaterials by periodic piezoelectric arrays with high-order resonant circuit shunts *Smart Mater. Struct.* **24** 065021

[27] Zheng Y, Zhang J, Qu Y and Meng G 2022 Investigations of a piezoelectric metastructure using negative-resistance circuits to enhance the bandgap performance *J. Vib. Control* **28** 2346–56

[28] Wang G and Chen S 2015 Large low-frequency vibration attenuation induced by arrays of piezoelectric patches shunted with amplifier–resonator feedback circuits *Smart Mater. Struct.* **25** 015004

[29] Wang G, Wang J, Chen S and Wen J 2011 Vibration attenuations induced by periodic arrays of piezoelectric patches connected by enhanced resonant shunting circuits *Smart Mater. Struct.* **20** 125019

[30] Wang G, Cheng J, Chen J and He Y 2017 Multi-resonant piezoelectric shunting induced by digital controllers for

subwavelength elastic wave attenuation in smart metamaterial *Smart Mater. Struct.* **26** 025031

[31] Sugino C, Ruzzene M and Erturk A 2020 Digitally programmable resonant elastic metamaterials *Phys. Rev. Appl.* **13** 061001

[32] Alfahmi O, Sugino C and Erturk A 2022 Duffing-type digitally programmable nonlinear synthetic inductance for piezoelectric structures *Smart Mater. Struct.* **31** 095044

[33] Zhang X, Yu H, He Z, Huang G, Chen Y and Wang G 2021 A metamaterial beam with inverse nonlinearity for broadband micro-vibration attenuation *Mech. Syst. Signal Process.* **159** 107826

[34] Li X, Chen Y, Hu G and Huang G 2018 A self-adaptive metamaterial beam with digitally controlled resonators for subwavelength broadband flexural wave attenuation *Smart Mater. Struct.* **27** 045015

[35] Silva T M P, Clementino M A, de Sousa V C and De Marqui C 2020 An experimental study of a piezoelectric metastructure with adaptive resonant shunt circuits *IEEE/ASME Trans. Mechatronics* **25** 1076–83

[36] Airoldi L and Ruzzene M 2011 Design of tunable acoustic metamaterials through periodic arrays of resonant shunted piezos *New J. Phys.* **13** 113010

[37] Ding H and Chen W 2001 *Three Dimensional Problems of Piezoelasticity* (Nova Science Publishers)

[38] Sugino C, Leadenham S, Ruzzene M and Erturk A 2017 An investigation of electroelastic bandgap formation in locally resonant piezoelectric metastructures *Smart Mater. Struct.* **26** 055029

[39] Sugino C, Ruzzene M and Erturk A 2018 Merging mechanical and electromechanical bandgaps in locally resonant metamaterials and metastructures *J. Mech. Phys. Solids* **116** 323–33

[40] Jian Y, Tang L, Hu G, Li Z and Aw K C 2022 Design of graded piezoelectric metamaterial beam with spatial variation of electrodes *Int. J. Mech. Sci.* **218** 107068

[41] Hu G, Austin A C, Sorokin V and Tang L 2021 Metamaterial beam with graded local resonators for broadband vibration suppression *Mech. Syst. Signal Process.* **146** 106982

[42] Alshaqaq M and Erturk A 2020 Graded multifunctional piezoelectric metastructures for wideband vibration attenuation and energy harvesting *Smart Mater. Struct.* **30** 015029

[43] Shengbing C, Jihong W, Gang W, Dianlong Y and Xisen W 2012 Improved modeling of rods with periodic arrays of shunted piezoelectric patches *J. Intell. Mater. Syst. Struct.* **23** 1613–21

[44] Wang X, Wang L, Shu H and Zhang L 2022 Research on dual-functional characteristics of piezoelectric metamaterial beams for vibration reduction and power generation *AIP Adv.* **12** 025326

[45] Yoon H, Youn B D and Kim H S 2016 Kirchhoff plate theory-based electromechanically-coupled analytical model considering inertia and stiffness effects of a surface-bonded piezoelectric patch *Smart Mater. Struct.* **25** 025017

[46] Sugino C, Ruzzene M and Erturk A 2018 Design and analysis of piezoelectric metamaterial beams with synthetic impedance shunt circuits *IEEE/ASME Trans. Mechatronics* **23** 2144–55

[47] Jian Y, Tang L, Hu G, Wang Y and Aw K C 2022 Adaptive genetic algorithm enabled tailoring of piezoelectric metamaterials for optimal vibration attenuation *Smart Mater. Struct.* **31** 075026

[48] Tang J and Wang K W 2001 Active-passive hybrid piezoelectric networks for vibration control: comparisons and improvement *Smart Mater. Struct.* **10** 794

[49] Norton M P and Karczub D G 2003 *Fundamentals of Noise and Vibration Analysis for Engineers* (Cambridge University Press)

[50] Chen T, Sorokin V, Tang L, Chen G and He H 2023 Identification of linear time-varying dynamic systems based on the WKB method *Arch. Appl. Mech.* **93** 2449–63

[51] Chen T, He H, He C and Chen G 2019 New parameter-identification method based on QR decomposition for nonlinear time-varying systems *J. Eng. Mech.* **145** 04018118